Journal of Thermal Science

https://doi.org/10.1007/s11630-022-1578-9

Processing Compressed Expanded Natural Graphite for Phase Change Material Composites

Alexander BULK*, Adewale ODUKOMAIYA, Ethan SIMMONS, Jason WOODS

National Renewable Energy Laboratory, 15013 Denver West Parkway, Golden, CO 80401, USA

Abstract: Phase change materials (PCMs) are used in various thermal energy storage applications but are limited by their low thermal conductivity. One method to increase conductivity involves impregnating organic PCMs into highly porous conductive matrix materials. Of these materials, compressed expanded natural graphite (CENG) matrices have received the most attention. Despite this attention, the effect that CENG processing has on PCM saturation and overall matrix thermal conductivity has not been fully investigated. Therefore, the effect of the heat treatment process used to expand intercalated graphite flakes is evaluated here.

Higher heat treatment temperatures yielded higher saturation rates and overall saturation at similar matrix porosities. For example, increasing temperature from 300°C to 700°C resulted in approximately 60%–70% increase in pore saturation after 100 minutes of soaking. The exposure time to heat treatment had less of an effect on PCM saturation. The exposure time had negligible effect above 30 min and above 500°C heating temperatures. However, because the expanded graphite was found to oxidize around 700°C, the use of longer exposure time in manufacturing applications can be beneficial if a shortened impregnation time is needed. Heat treatment conditions did not impact thermal conductivity. The composite latent heat of fusion was also reduced approximately proportionally to the PCM mass fraction. A local maximum in axial thermal conductivity was observed at around 83% porosity, which is similar to previous studies. The observed conductivity at this maximum was a factor of 81 times greater than the conductivity of the PCM.

Keywords: phase change materials, thermal energy storage, compressed expanded natural graphite, thermal conductivity enhancement, porous material sorptivity, composite matrix

1. Introduction

Porous graphite matrices can be used for a variety of energy material applications [1–3]. Particularly, they are used to enhance the thermal conductivity of phase change materials (PCMs), which store and release a large amount of latent thermal energy at their phase transition temperature [4–9]. Organic PCMs are commonly used for thermal management applications. They possess high latent heat of fusion, are noncorrosive, and are stable over many charge/discharge cycles, but suffer from low thermal conductivity (0.1–0.3 W/(m·K)) [10–18]. This significantly limits their charging and discharging rates.

Thermal energy storage applications involving organic PCMs include concentrated solar power storage [19–21], thermal management in electronics [22–24], and electric

Received: Feb 24, 2021 AE: GUO Shaopeng Corresponding author: Alexander BULK E-mail: alexander.bulk@nrel.gov

Glossary and Symbols

CENG	Compressed Expanded Natural Graphite
Effective porosity	the percentage of total volume void of material that is accessible and not closed off from the outside of the material
Graphite worms	graphite flakes that have been intercalated with acid and heat treated, causing them to expand
Hexadecane	an organic alkane PCM with a phase transition near room temperature
HVAC	Heating, Ventilation, and Air-Conditioning
Latent heat of fusion	the amount of energy required to change the state of a substance between solid and liquid at constant pressure
PCM	Phase Change Material
PCM/CENG composite	a composite matrix of CENG impregnated with PCM
Porosity	the percentage of total volume void of material
Sorptivity	A measure of the capacity of a material to absorb or desorb a liquid via capillary force
Tetradecane	an organic alkane PCM with a phase transition temperature useful to HVAC applications
Thermal conductivity	the amount of heat that flows through a unit of area by one degree per unit distance
Tortuosity factor	the ratio of the length of fluid diffusion through a porous media to the fluid displacement length

List of Symbols

A	cross-sectional area perpendicular to the direction of 1-D soaking/cm^2
B	sorptivity model constant/g
K_S	the sorptivity/g·cm^{-2}·s$^{-1/2}$
m	mass of saturating liquid/g
m_{CENG}	mass of CENG/g
m_{PCM}	mass of PCM/g
r_0	average pore radius/cm
t	time/s
V_{CENG}	volume of CENG/cm^3
V_f	volume fraction of PCM/%
$V_{f,PCM}$	percent of total pore volume filled with PCM/%
γ	surface tension/g·s^{-2}
δ	bulk CENG density/g·cm^{-3}
ε	effective porosity/%
η	fluid viscosity/g·cm^{-1}·s^{-1}
θ	liquid contact angle to the pore walls/(°)
λ	tortuosity factor
ρ	fluid density/g·cm^{-3}
ρ_{CG}	crystalline graphite density/g·cm^{-3}
ρ_{PCM}	PCM density/g·cm^{-3}
φ	CENG porosity/%

vehicle battery thermal management [25–28]. However, organic PCMs have received greater attention in applications involving thermal management of buildings. They can be used for regulating passive heat transfer in building envelopes [29–33] or used in heat exchangers for active space heating or cooling in HVAC systems [34, 35].

One method used to enhance the PCM thermal conductivity is to insert it into porous, thermally conductive host matrices, such as metallic or graphitic foams [36–44]. Compressed expanded natural graphite (CENG) is of particular interest due to its low cost, high porosity, small (nano/micro) pore size, high pore density, high thermal conductivity, and ability to be molded into many geometries [44–47]. Literature has shown that infiltrating CENG with PCM can improve the PCM conductivity by more than a factor of 100 [4, 5, 38, 43, 48, 49]. CENG/PCM composite properties are affected by the CENG manufacturing process. However, the effect of key processing parameters has not been fully investigated. The graphite/PCM composite manufacturing process is described in detail in Ref. [48]. The process includes four major steps:

First, graphite flakes are made into expandable graphite by intercalating sulfuric and/or nitric acid between the graphene layers. Second, these graphite intercalated compounds are heat-treated, causing the intercalated acid to transition to a gas [50, 51]. The acidic gases force the graphene layers to partially separate,

generating accordion-shaped particles referred to as graphite "worms" [52]. Third, to form the CENG matrix, the expanded graphite "worms" are compacted to any desired bulk density greater than 50 g/L (97.6% porous) [48]. Lastly, the PCM is impregnated into the CENG matrix via soaking, resulting in a PCM/CENG composite material. The rate at which PCM saturates the CENG pores is sensitive to the processing parameters, namely the heat treatment temperature and exposure time. Therefore, the effect of these two parameters is investigated here.

A few major studies have previously investigated the thermal conductivity of CENG matrices and their ability to be impregnated by different PCMs. However, these studies did not fully examine the effect of CENG processing parameters. Py et al. first examined the rate of hexadecane impregnation into CENG of various porosities. They used these results to develop a model to predict PCM penetration depth [4]. At lower porosities (<83%), a significant amount of pore space was left unsaturated, which was assumed to be caused by the high compaction creating closed (isolated) pores.

In this same study, the authors measured axial and radial conductivity versus porosity in both the pure CENG and PCM/CENG composite using a guarded hot plate. The thermal conductivities of the pure and composite CENG matrices were found to be nearly the same. Later, Bonnissel et al. expanded on this study to evaluate conductivity across a greater range of CENG porosities [50]. Thermal conductivity was calculated by measuring the thermal diffusivity via the flash method and the specific heat capacity via calorimetry. The results were used to model local conductivity and permeability under uniaxial compression. From this study, it was found that CENG matrices exhibit isotropic conductivity up to 50 kg/m^3 (97.6% porosity), and local conductivity becomes anisotropic at higher bulk density (lower porosity).

More recently, Mallow et al. studied the thermal conductivities of CENG matrices with different porosities after saturating them with various organic paraffins [45]. A setup similar to the guarded hot plate method was used to measure thermal conductivity, which contained a heat source on one side of the sample. However, ambient conditions acted as the heat sink on the other side. Thermal conductivities in the axial direction were found to be much greater than those measured in previous studies, reaching 10 W/(m·K) at porosities as high as 93%. For comparison, Py et al. and Bonnissel et al. measured 5 W/(m·K) and 4.2 W/(m·K) at this porosity, respectively, and a maximum of about 7 W/(m·K) and 8.7 W/(m·K) at 80% [4, 50]. It is unclear why these differences were observed. They could be related to the expansion or compaction method or the methods used to measure conductivity. Some studies used microwave radiation to induce expansion [22, 33]. However, a constant-temperature heat treatment is not provided by this method. The fact that Py et al. purchased pre-expanded graphite, whereas Mallow et al. expanded graphite in a microwave reactor at a constant heat flux, likely also contributed to differences. The compaction methods used may also affect the matrix morphology, which impacts phonon scattering.

In each of these studies, the only processing parameter examined was the matrix bulk density/porosity. To the authors' knowledge, no research has considered the effects of expansion heat treatment parameters, including temperature or exposure time, on PCM saturation. Only a single study (Han et al.) measured the effect of heat-treatment temperature on CENG thermal conductivity [53]. However, the effects of exposure time were not considered. In this study, conductivity was measured using a custom transient technique. It is known that transient techniques have challenges with measuring the thermal conductivity of porous, nonhomogeneous matrices [54–56]. In this case, a very small sample size (5 mm×5 mm×(10–20) mm) on a scale of the individual graphite worms further exacerbated these challenges. Han et al. found no difference in conductivity between samples heat-treated at different temperatures.

To our knowledge, the effect of CENG processing parameters on PCM saturation has ever been examined. Likewise, the effect of processing parameters on the thermal conductivity of bulk CENG has not been evaluated using reliable measurement methods. In this study, we investigate the thermal CENG processing parameters to understand their impact on PCM saturation and thermal conductivity. Saturation and conductivity directly impact the power and energy density of PCM/CENG composite. Power density is the rate of energy transferred per unit volume, and energy density is the energy stored per unit volume. Power density is improved with the higher conductivity of the graphite matrix, while energy density is improved by maximizing the pore saturation of the CENG matrix [18, 46]. Because previous studies have shown that the thermal conductivities of the CENG matrix alone and the PCM/CENG composites are nearly the same [4], we measured only the thermal conductivity of the CENG matrix. Pore saturation was measured at different PCM soaking time intervals. The latent heat of fusion of the composite was also evaluated at different PCM/mass ratios. However, accuracy was limited because of the small sample size required under differential scanning calorimetry (DSC). Tetradecane was used as the PCM due to its high latent heat (215.23 J/g) [57] and phase change temperature around 4°C–6°C, which is of interest for air-conditioning applications [9, 17].

2. Materials and Methods

We used commercially available expandable graphite with an average flake size of 177 microns and sulfuric acid as the intercalating agent (ACS Material EG-150-230). The intercalated raw material was washed and neutralized to pH 7 before shipment. Tetradecane with a purity of 99% was procured from Sigma-Aldrich Corporation.

This study focused on the impact of thermal treatment, namely temperature and exposure time, on the morphology, PCM impregnation, and thermal conductivity of the produced CENG matrix. The morphology was studied using an FEI Quanta 600 Scanning Electron Microscope (SEM). PCM impregnation was evaluated by measuring pore saturation as described below.

2.1 Compressed Expanded Natural Graphite (CENG) matrices

The CENG samples were created through the method shown in Fig. 1. The samples for PCM saturation were prepared with 1.5 g of expandable graphite, whereas those for thermal conductivity measurement were prepared with a higher mass (required to reach the desired 4.5-mm thickness at each porosity). 10 mg of CENG was used for samples prepared for calorimetry. The expandable graphite was weighed in a quartz beaker, and then placed in a preheated MTI Corporation KSL-1200X furnace and left inside for the desired exposure time. Table 1 shows the heat treatment temperatures and exposure time for the saturation rate experiments (identified with an "X"), thermal conductivity measurements (identified with a "T"), and latent heat of fusion measurements (identified with an "H"). The expanded graphite was then allowed to cool for 15 to 30 minutes at room temperature prior to compression.

Thermal conductivity was measured using a guarded heat flow instrument (TA Instruments DTC 300 Guarded Heat Flow Meter), which requires 50-mm diameter samples over 4-mm thick. Therefore, a custom-machined pellet die was used to prepare 4.5-mm thick CENG samples. A 40-mm diameter Carver pellet die was used to prepare samples for PCM saturation. Latent heat of fusion was measured using a DSC (TA Instruments DSC 2500) which used approximately 5-mm diameter calorimeter pans. Therefore, a 3.175-mm diameter Carver pellet die was used to prepare DSC samples. To compress samples to a given porosity/bulk density, a Carver hydraulic press (Model #3912) with digital force readout was used with the 40-mm Carver pellet die, and a Grizzly Industrial H6231Z 10-ton benchtop hydraulic press was used with the custom die. The 3.175-mm die was compressed manually.

The compression force required to generate a given porosity/bulk density was calibrated using several 40-mm diameter samples (Fig. 2). The 50-mm diameter samples were formed by compressing to a point marked on the die indicating a 4.5-mm thickness, and the desired porosity was obtained by loading the respective mass of graphite. The reverse was done for the 3.175-mm diameter samples, which were compressed to a point marking a desired porosity based on measured mass. Mass was measured using a Mettler Toledo XS104 analytical mass balance (±0.05 mg). The thickness of the disk-shaped CENG matrices, or "pucks," were measured with a caliper (±0.005 mm). We calculated bulk density (δ) and porosity (φ) using Eqs. (1) and (2). Volume was calculated assuming a 40- or 50-mm diameter cylinder with uniform thickness. The porosity calculation is based on the density of crystal graphite, which is taken as ρ_{CG} = 2.09 g/cm^3 [58].

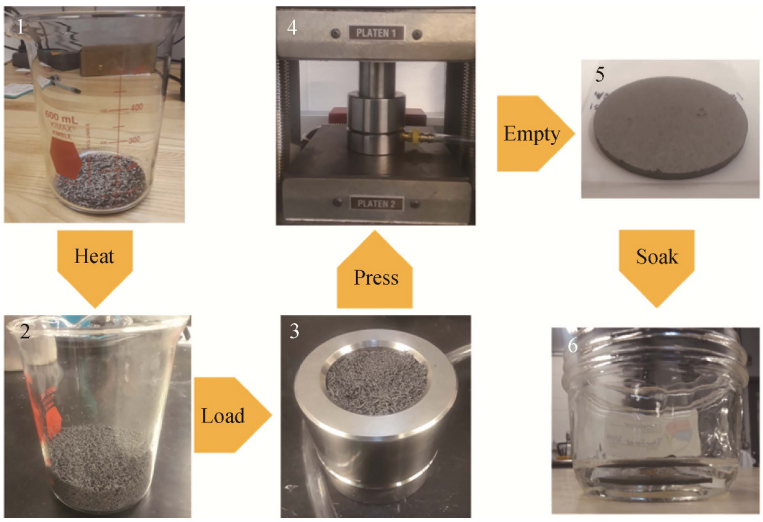

Fig. 1 Flowchart depicting procedure for creating CENG/PCM matrices

$$\delta = \frac{m_{\mathrm{CENG}}}{V_{\mathrm{CENG}}} \tag{1}$$

$$\varphi = 1 - \frac{\delta}{\rho_{\mathrm{CG}}} \tag{2}$$

Table 2 provides a description of the procedure used to prepare CENG samples shown in Fig. 1. Using the Carver hydraulic press calibration curve (Fig. 2), 40-mm diameter pucks with 65% and 95% porosity were produced with approximately 1764 N and 39 N compression force, respectively.

For thermal conductivity measurements, porosities of approximately 65%, 75%, 83%, and 90% were examined. Above 90%, the 50-mm samples had very low binding force and the samples often fell apart. However, the 40-mm samples prepared to measure saturation rate were able to hold together at 95%. This was due to their smaller diameter, and because they were not under pressure in the thermal conductivity instrument. The lower porosity (65%) was selected because it was difficult to pack expanded graphite homogenously below that value. Variability in local density was generated in the pucks compressed to porosities below 65% that would force them to split into layers.

Table 1 Heat treatment temperatures and exposure time used for analyzing CENG matrix saturation rates (X), thermal conductivity (T), and latent heat of fusion (H)

Exposure time/ min	Heat treatment temperatures/°C			
	300	400	500	700
5	X, T	X	X, T, H	X, T
30	X	X	X	X
60	X	X	X	X
120	X	X	X	X

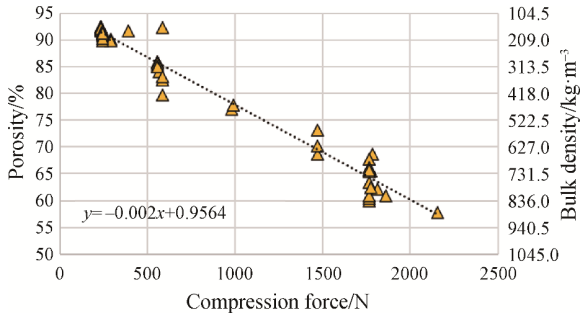

Fig. 2 Correlation between CENG matrix porosity and compression force

Table 2 Description of CENG sample preparation procedure shown in Fig. 1

Step (Fig. 1)	Saturation/Latent Heat of Fusion Experiments
1	Prepare 1.5 g of expandable graphite in beaker
2	Heat at desired temperature and exposure time in furnace
3	Load expanded graphite into 40-mm diameter pellet die
4	Compress sample with Carver hydraulic press
5	Remove sample from pellet die/measure thickness and mass
6	Soak in PCM for desired time
Step (Fig. 1)	**Thermal Conductivity Experiments**
1	Prepare mass of expandable graphite in beaker to achieve 4.5-mm thickness at desired porosity
2	Heat at desired temperature and exposure time in furnace
3	Load expandable graphite into 50-mm diameter pellet die
4	Compress sample with Grizzly hydraulic press
5	Remove sample from pellet die/measure thickness and mass
6	n/a

The small size of the 3.175-mm samples caused them to become fragile when soaked in PCM at high porosities. High porosities also required preparing masses of CENG too low to accurately weigh. Therefore, these samples were prepared at porosities of 49%, 58%, and 64%.

2.2 Phase Change Material (PCM) impregnation

To saturate the porous CENG with PCM, the 40-mm diameter CENG pucks were submerged in a beaker of tetradecane over 75 000 minutes, although 100% saturation occurred much earlier in most samples. Tetradecane is liquid at room temperature, allowing the pucks to be saturated via simple soaking. The CENG puck was removed with tweezers at regular time intervals, patted dry to remove excess PCM on the exterior surfaces, and weighed. This was done to measure the change in mass of the PCM in the pores over the time interval. Patting was controlled to ensure equivalent removal of surface PCM between samples. The small pore size and strong capillary force induced prevented PCM from leaking from the CENG when drying.

The PCM volume fraction (%) was determined by calculating the volume of PCM loaded at each time interval. The saturated PCM mass was divided by the room temperature density of tetradecane [57], and the CENG volume, according to Eq. (3):

Table 3 CENG PCM saturation time measurement intervals (unit: min)

Time 1	Time 2	Time 3	Time 4	Time 5	Time 6	Time 7	Time 8	Time 9	Time 10	Time 11	Time 12	Time 13
0	0.5	1	3	10	30	100	300	1500	3000	10 100	30 200	75 000

$$V_{\mathrm{f}} = \frac{m_{\mathrm{PCM}}}{\rho_{\mathrm{PCM}} \cdot V_{\mathrm{CENG}}} \quad (3)$$

We then calculated the percent pore saturation, or the fraction of pore space filled with PCM using Eq. (4):

$$V_{\mathrm{f,PCM}} = \frac{V_{\mathrm{f}}}{\varphi} \quad (4)$$

Measurements were performed at time intervals that scaled relatively logarithmically but were adjusted to fall within laboratory operating hours (Table 3).

2.3 Thermal conductivity measurement

The TA Instruments DTC 300 Guarded Heat Flow Meter measures 50-mm diameter samples with thermal resistances between 0.0005 and 0.01 $m^2 \cdot K/W$ at an accuracy of ±3%. Based on the conductivities measured in previous studies [4, 45, 50], we prepared samples to a target thickness of 4.5-mm to fall within the thermal resistance range.

Thermal conductivity was measured across setpoints ranging from 20°C to 110°C. The DTC 300 holds the top stack (heat source) to a temperature 15°C above the setpoint temperature, and the bottom stack (heat sink) at 15°C below. Temperature is controlled to equilibrate at a 30°C difference between top and bottom stack, generating a sample temperature within a few degrees of the setpoint. CENG sample pucks were loaded into the instrument using a thin layer of silicone thermal joint compound (Wakefield Engineering Inc.) of 0.73 W/(m·K) thermal conductivity to reduce contact resistance between the stack surfaces. Contact resistance was also reduced by applying a pressure of 172 kPa from pneumatic control of the top stack.

The DTC 300 is regularly calibrated to a set of five samples of known thermal resistances. These samples consist of stainless steel and Vespel® Plastic at different thicknesses. Calibrations are performed across a range of temperatures from 0°C to 200°C.

2.4 Latent heat of fusion measurement

The 3.175-mm diameter CENG samples were submerged in tetradecane until fully saturated. Samples were then sealed inside hermetic calorimetry pans. The TA Instruments DSC 2500 ramps the temperature of the sample and reference at a specified rate across a specified temperature range (±0.005°C precision). Here, samples were heated at a rate of 5°C/min between –25°C and 35°C. This range was selected around the transition temperature of tetradecane (~4.5°C) [9, 17].

The DSC 2500 measures enthalpy accurately within ±0.04%. Samples were cycled three times across the temperature range between heating and cooling to calculate standard error. The DSC 2500 is regularly calibrated to indium and sapphire samples of known thermal resistances. Calibrations are conducted specific to the temperature ramp rate used. The enthalpy of fusion of pure tetradecane was verified with NIST-reported values [59] prior to conducting measurements.

3. Results and Discussion

3.1 Temperature and exposure time effect on PCM impregnation

Fig. 3 shows transient PCM pore saturation data for CENG with approximately 95% porosity. Results show that higher heat treatment temperature and exposure time yields higher rates of saturation and greater maximum saturation. Although samples were patted dry to remove excess PCM on the CENG pucks' surfaces, some residual PCM resulted in maximum saturation measured above 100% of the available pore volume.

Higher heat treatment temperature increases PCM saturation rates, evidenced by the slope increase with temperature in Fig. 3. At 100 min, there is an approximately 60%–70% increase in pore saturation between 300°C and 700°C temperatures, depending on the heat treatment exposure time. At low heating temperature, CENG saturation increases initially but then plateaus at 20%–50% saturation from around 30 s until 100 min. The cause of this plateau is unclear. However, saturation continues to steadily increase after approximately 100 min. When heated at higher temperatures, the pucks initially saturate at a rapid, apparently exponential rate until saturation plateaus near 100% around 1–100 min.

PCM saturation was affected differently in the 65% porous samples (Fig. 4) than the 95% samples at low heat treatment temperatures. Instead of seeing rapid saturation followed by a plateau, the saturation rates were nearly linear for the duration of the 75 000 min PCM impregnation time. This difference was expected, since in order to achieve 100% pore saturation, the 65% porous samples had to absorb 54.7% of their initial mass (0.81 g of tetradecane), whereas 95% porous samples absorbed 33.3% of their initial mass (0.50 g of tetradecane).

At both porosities, heat treatment exposure time increased saturation but had diminishing returns. The 65% porous/500°C samples with 5 min heating reached 90% saturation around 1000 min. When heated for 30 min, 90% saturation was obtained within 20 min. However, longer exposure time reduced the time to 90% saturation only slightly further. At lower heat treatment temperatures, the exposure time had a greater impact. At the end of the experiment, the 300°C-heated samples reached only 40% for 5 min heating, but around 80% for longer heating time.

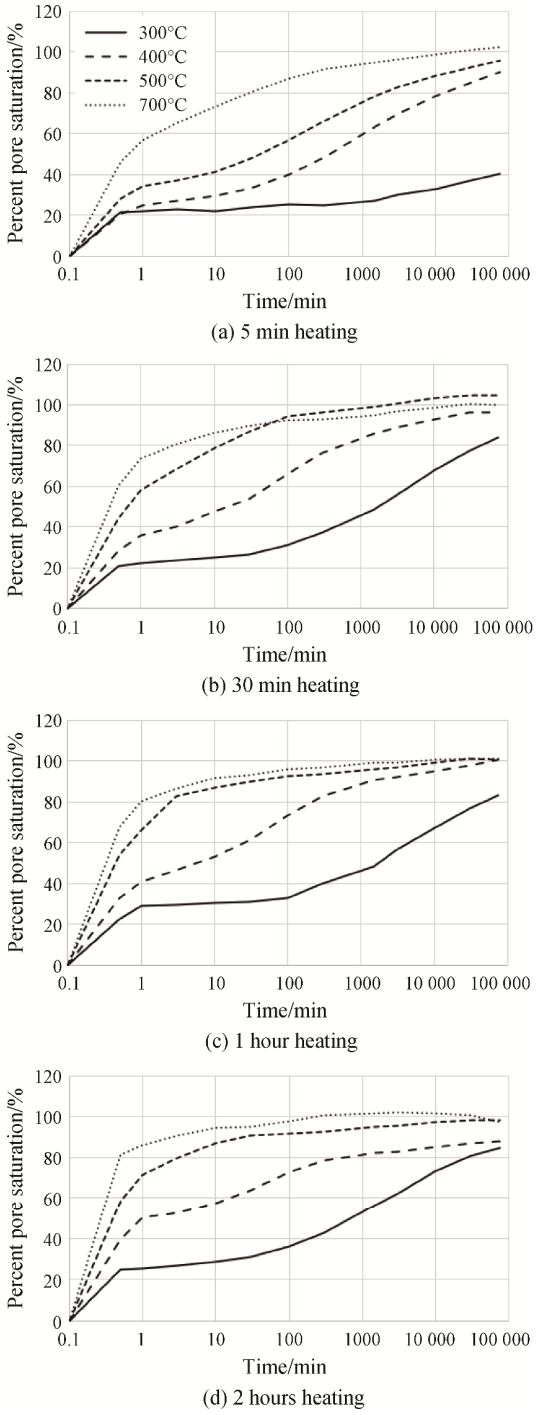

Fig. 3 Saturation curves of tetradecane in 95% porous CENG pucks heated for: (a) 5 min; (b) 30 min; (c) 1 h; (d) 2 h

The pore saturation curves in Figs. 3 and 4 are partially supported by a model developed by Beltran et al. to estimate the saturation rate of various liquids into porous ceramics (Eq. (5)) [60, 61]. Inagaki et al. previously verified this model in expanded graphite saturated by oils of varying viscosity [61]. Here, we have seen a similar response to the rate of tetradecane saturation. The model states that the added mass of saturating liquid (m) per cross-sectional area (A) perpendicular to the direction of one-dimensional soaking is expressed as a function of time (t):

$$m = AK_S\sqrt{t} + B \tag{5}$$

where B is a constant and K_S is the sorptivity (g/(cm^2·s$^{1/2}$)). The sorptivity K_S is given as:

$$K_S = \left(\rho\sqrt{\frac{\gamma}{\eta}}\right)\left(\frac{\varepsilon}{\lambda}\sqrt{r_0}\right)\left[\sqrt{\frac{\cos(\theta)}{2}}\right] \tag{6}$$

where ρ is the fluid density (g/cm^3); γ is surface tension (g/s^2); η is fluid viscosity (g/(cm·s)); ε is the effective porosity (%); λ is the tortuosity factor (unitless); r_0 is the average pore radius (cm); and θ is the liquid contact angle to the pore walls (°). Here, ρ, γ, η and θ are constant, but r_0, λ and ε are likely affected by the heat treatment temperature and exposure time, influencing K_S.

The saturation curves shown in Fig. 3 resembled the saturation model in Eq. (5) at low temperature and heat treatment time. Because the model is based on an infinitely-sized porous medium, this resemblance occurred only during the region in which an upward concave is shown. However, since the CENG pucks exhibit finite volume, experimental results plateau while nearing 100% saturation. If we assume that K_S changes with time, then the above data still follows this equation. This would occur from PCM filling large pores first, and then filling regions with smaller r_0, higher λ, and lower ε in Eq. (6) [60], causing K_S to gradually decrease until the PCM fully saturates the graphite. Because the samples were soaked from all sides in a PCM bath, the cross-sectional area of the sorption front (A) would also decrease as the sample would become more saturated. The 65% porous samples also followed this trend initially (t<30 min) at low temperatures (Fig. 4).

Fig. 5 shows the isolated effect of exposure time on samples expanded at 500°C, which illustrates the diminishing returns highlighted above. Within the first 10 min of soaking, total saturation increases with exposure time for all samples but plateaus after 60 min of heating. Increasing heat treatment exposure time from 5 min to 30 min yielded a 40% increase in pore saturation, whereas increasing to 60 min generated less than an additional 10% increase. After 1500 min soaking, all 500°C samples were fully saturated when heated more than 5 min. This suggests that exposure time greater than 30 min will not improve final saturation if allowed a day or more for PCM impregnation.

Increasing heat treatment temperature continues to improve saturation rates and overall saturation. However, increasing heat treatment exposure time only improves total saturation for short PCM soaking time, heating time less than 30 min, or for heating temperatures less than

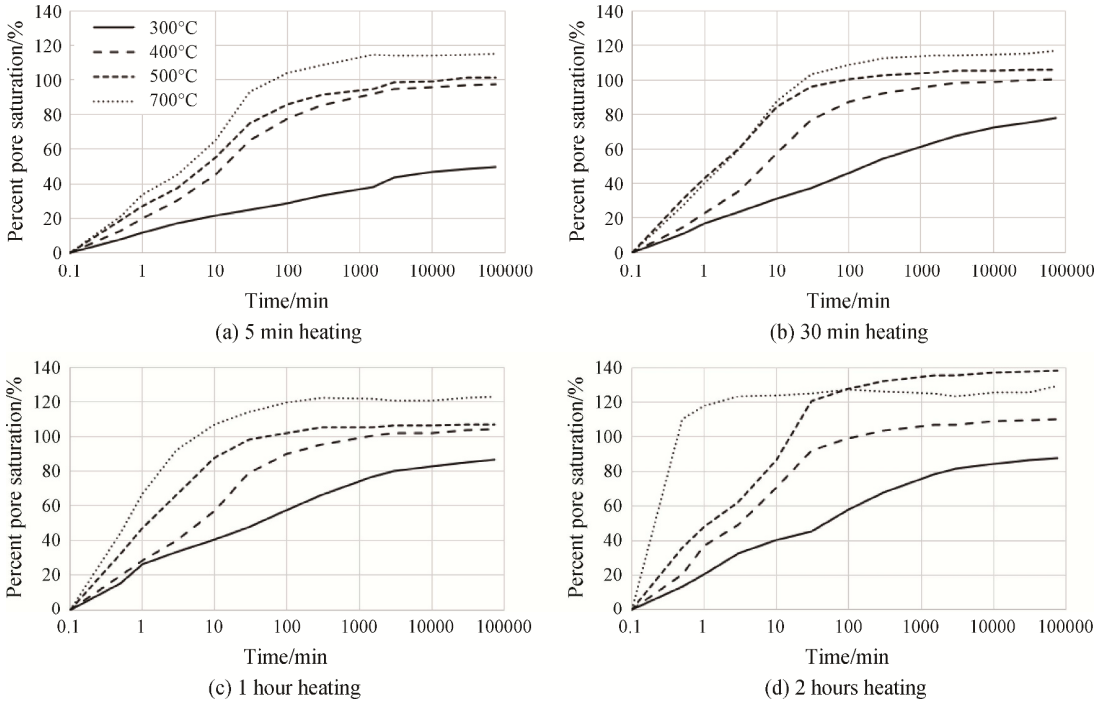

Fig. 4 Saturation curves of tetradecane in 65% porous CENG pucks heated for: (a) 5 min; (b) 30 min; (c) 1 hour; (d) 2 hours

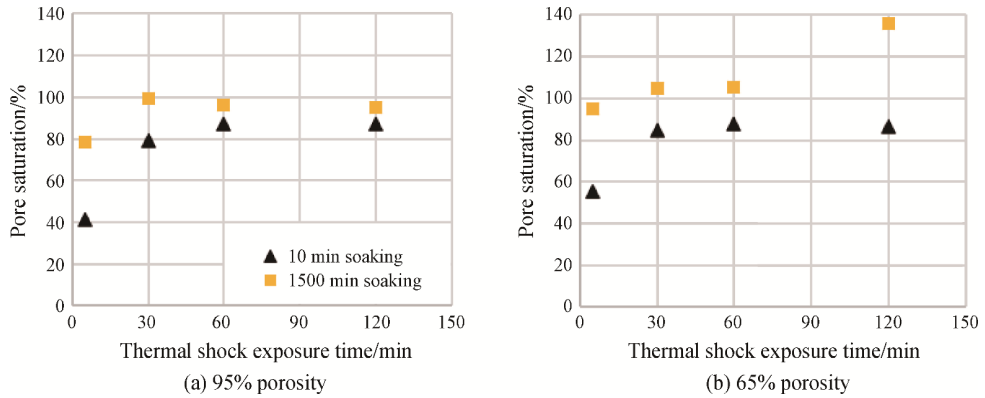

Fig. 5 Maximum tetradecane saturation in porous CENG expanded at 500°C

500°C. This will prove beneficial for manufacturers unable to soak PCM composites for long durations in an industrial setting, in which heat treatment temperature and/or heating exposure time can be increased to compensate. For example, instead of soaking a 95% porous sample heated at 300°C for 30 min (Fig. 3(b)) to 80% saturation, which would take over 33 days, the heat treatment temperature could be increased to 700°C in order to achieve the same saturation within 2.5 min. We have found that heating temperature can only be increased up to 700°C, beyond which graphite begins to oxidize and its physical and chemical properties are altered. In the cases where both soaking time and heat treatment temperature are limited, heat treatment exposure time can be increased to compensate.

3.2 Temperature and exposure time effect on CENG matrix morphology

SEM images of expanded graphite worms heat-treated at different conditions are shown in Fig. 6. When comparing the graphite expanded at 300°C and 500°C, only subtle morphological differences appear. For example, the pore openings in the 300°C expanded graphite appear more ordered and uniform than the 500°C expanded graphite, and the 500°C expanded graphite appears to have more pores per unit length than the 300°C expanded graphite. When comparing the 500°C graphite expanded for 30 min and 5 min, we see that the 30-min-heated graphite exhibits greater pore density than when heated for 5 min. This greater pore density may be associated with improved saturation, as

described in Eq. (6), due to larger pores and higher effective porosity.

When heat treated at 700°C for long exposure time, a significant amount of material appears visibly red to the naked eye, indicating the graphite begins to oxidize around this temperature. SEM images of expanded graphite heated to 700°C show pores of irregular shape and variable size. Some of the pores generated at this temperature are much larger than pores generated by expansion at 500°C. This could potentially be caused by partial oxidation of the graphite, further opening pores and generating additional space for PCM. It is difficult to discern from these images whether effective porosity has changed between 500°C and 700°C, but it is clear that individual pore size increased. Based on the model described in Eq. (6), this would also improve sorptivity by increasing average pore radius and decreasing the tortuosity factor [60].

Han et al. evaluated the effect of heat treatment temperature on the open porosity of CENG [53]. These measurements were performed using helium pycnometry, which measures the displaced helium that is pressurized through the matrix [53]. Results suggested that accessible pore volume increases with heat treatment temperature, which could partially explain the higher PCM saturation with temperature. More accessible pore volume is equivalent to a higher effective porosity and would also likely reduce the tortuosity factor. There is a need for better understanding of CENG pore morphology to better ascertain the relationship between K_S and heat treatment conditions.

3.3 Temperature effect on CENG matrix thermal conductivity

The average CENG thermal conductivity at 20°C with respect to porosity is shown in Fig. 7 alongside the results from past studies [45, 50] and the Py et al. model with associated uncertainty (unc.) [4]. The results from Han et al. were not included because only the accessible pore volume was calculated [53]. Data from Bonnissel et al. and Mallow et al. were from individual samples, whereas data from Py et al. was attained from a model fit to experimental data.

Because the DTC temperature would not equilibrate to the exact setpoint, the conductivity at 20°C was determined via interpolation. Three to five measurements

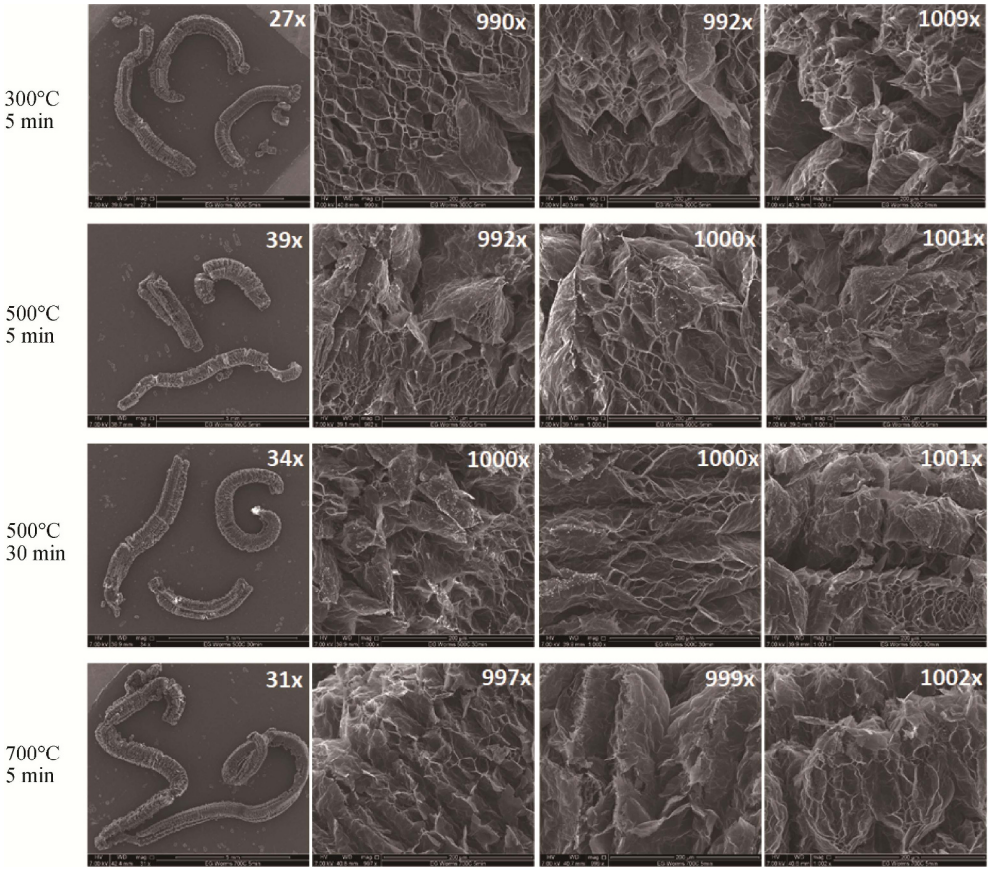

Fig. 6 SEM images of expanded graphite heat-treated at various temperatures. Rows: increasing heat treatment temperature from top to bottom. Columns: different SEM magnification

were performed using each CENG puck from which the average conductivity was calculated. Error bars signify the standard deviation between measurements. Here, only the effect of heat treatment temperature was evaluated as the exposure time was held to five minutes. Samples were prepared to mean porosities of 66.5%, 76.4%, 83.7%, and 91.9%. When comparing these values, the different methods used to prepare CENG, as well as to measure thermal conductivity, should be considered.

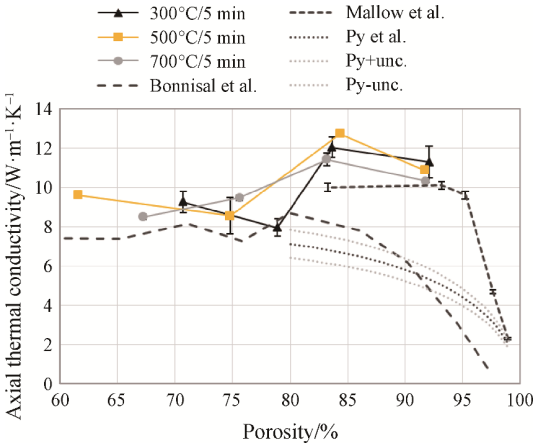

Fig. 7 Effect of heat treatment temperature on CENG thermal conductivity versus porosity

Although thermal conductivity is shown to vary significantly with CENG porosity, heat treatment temperature did not appear to influence thermal conductivity. No statistically significant difference in thermal conductivity between samples heated at different temperatures was measured at similar porosities. The thermal conductivity of samples heated at 300°C and 500°C followed the same general trend, in which the conductivity exhibited a slight decrease from 60% to 80% porosity prior to reaching a maximum conductivity at around 83% porosity. However, samples heated to 700°C exhibited a steady increase in conductivity to the 83% maximum porosity. The conductivity at this maximum ranged between 11.4 W/(m·K) (700°C) to 12.8 W/(m·K) (500°C), constituting an improvement in the thermal conductivity of tetradecane by a factor of over 81 [62].

The reduction in conductivity observed above 83% porosity is likely caused by the increase in the ratio of pore space to graphite volume. As the volume fraction of CENG is reduced, there are less conduction pathways through the graphite, thus reducing overall conductivity [46]. Reduction in the volume fraction of CENG does not, however, correlate with conductivity at porosities below 83%. As the graphite is compacted at greater force to achieve porosities below 83%, the worms flatten and extend in the radial direction, causing the anisotropy in the matrix. Higher compression aligns the graphite to stack in planes normal to the direction of compression. Thermal resistance from one plane to another is much higher than resistance within a single graphite plane, thus reducing conduction in the compression direction. Similar conditions occur in highly oriented pyrolytic graphite sheets, which are very high density graphite matrices [63]. The in-plane conductivity of these sheets is above 1000 W/(m·K), but the conductivity across the sheet (plane-to-plane conduction) is less than 6 W/(m·K). This observed maximum thermal conductivity around 83% porosity was also observed by Bonnissel et al., who measured a maximum conductivity at 80% porosity [50], although overall conductivity was slightly lower than measured here.

At lower porosities (below approximately 83%), the measured thermal conductivity was consistent with previous studies [4, 45, 50], except for Han et al., who found conductivity to improve as the porosity was lowered [53]. As discussed in the introduction, this could be attributable to the technique used to measure conductivity. Here, thermal conductivity at 83% and greater porosities was measured slightly above what was measured in previous literature. Because there was no observed difference in thermal conductivity between samples prepared via different heat treatment temperatures, these differences could potentially be associated with different methods used to measure conductivity or, potentially, different graphite material acquired from different manufacturers. Mallow et al. used a microwave reactor for heat treatment and Py et al. purchased pre-expanded graphite. Bonnissel et al. expanded graphite at the same temperatures used here but did not specify exposure time. It is unclear whether the different heat treatment methods (e.g., microwave reactor) would contribute to these differences in measured conductivity. However, because our results showed that heat treatment temperature does not appear to affect conductivity, we presume that the various materials and measurement methods used could be a significant contributing factor in this discrepancy. By calculating conductivity from separate measurements of heat capacity and diffusivity, Bonnissel et al. introduced added uncertainty. The lack of control over the heat sink temperature in Mallow et al.'s guarded heat flow meter may also hinder the ability of the sample to effectively achieve thermal equilibrium.

Fig. 8 shows the measured conductivity versus sample temperature. *Y*-axis error bars signify the standard deviation between repeated samples. The standard deviation in temperature between measurements is negligible and, therefore, *x*-axis error bars are not shown.

Regardless of the heat treatment temperature and porosity, conductivity increased with sample temperature

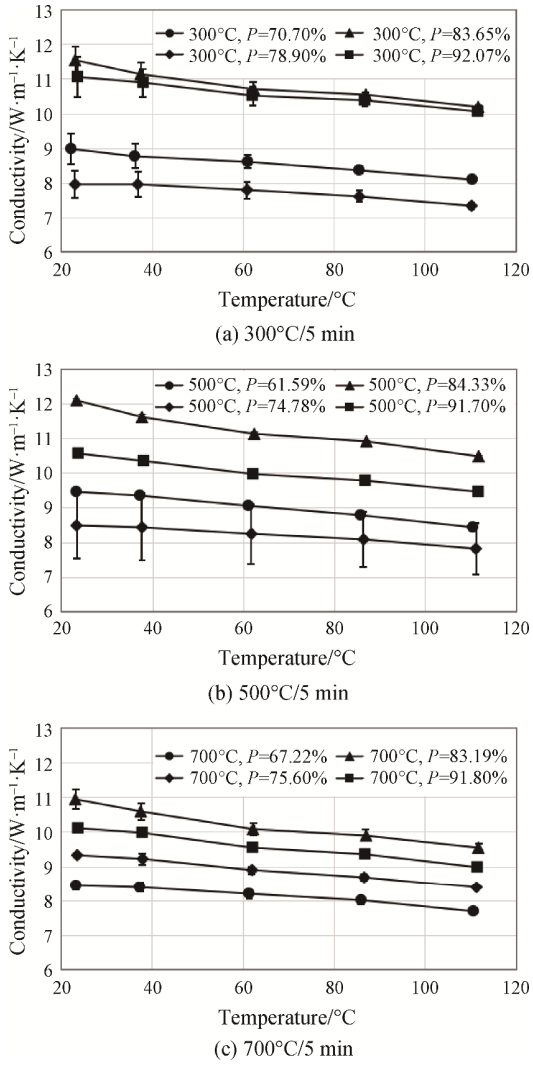

Fig. 8 Effect of CENG temperature on thermal conductivity using expanded graphite heated at: (a) 300°C/5 min; (b) 500°C/5 min; and (c) 700°C/5 min. *P* denotes sample porosity.

in every CENG matrix examined. This is due to increased phonon scattering with temperature for crystalline graphite [63].

3.4 Latent heat of fusion

The latent heat of fusion of fully saturated CENG is reported in Fig. 9(a) and compared with pure tetradecane at the same mass. Error bars indicate propagated uncertainty in the measured puck mass. Mean values are provided in Table 4 with sample volume and mass fractions. Samples were saturated to slightly over 100% due to residual PCM, so samples of equivalent porosity had different PCM mass fractions. The average latent heat of fusion was calculated from three consecutive heating/cooling cycles. Error bars signify the standard error across cycles.

Fig. 9(b) shows the latent heat of fusion normalized to the PCM mass fraction. Again, error bars indicate uncertainty propagation in measured mass. Here, we see that the latent heat of fusion of pure tetradecane is within the uncertainty of the measured composite latent heat of fusion for each sample. Therefore, these measurements did not indicate that the latent heat of fusion of the PCM was affected by its impregnation in the CENG matrix.

Table 4 CENG-PCM composite sample latent heat of fusion measurement parameters

Bulk porosity/%	48.9	57.9	64.3
Bulk volume/mm^2	10.2	12.5	14.7
CENG bulk mass/mg	10.9	11.0	11.0
PCM bulk mass/mg	3.9	5.7	8.3
% Mass PCM	26.4	34.1	43.0
% Pore Saturation	102.4	103.2	115.1
Mean Latent Heat of Fusion/J·g^{-1} (± standard error)	55.9 ±0.2	81.7 ±0.4	90.0 ±0.2
Latent Heat of Fusion/ PCM Mass Fraction/J·g^{-1} (± propagated uncertainty)	212.1 ± 63.5	239.3 ± 22.5	209.4 ±42.2

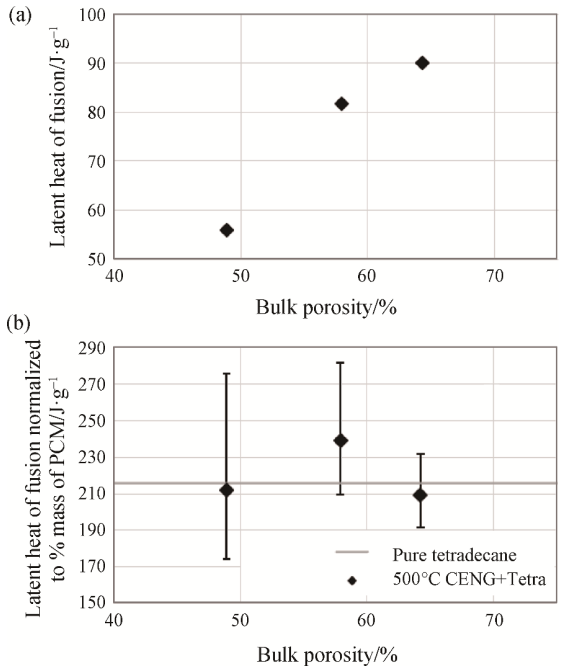

Fig. 9 CENG-PCM composite latent heat of fusion (a) and latent heat of fusion normalized to PCM mass fraction (b) compared with the latent heat of fusion of pure tetradecane [57]

4. Conclusions

Thermal energy storage requires both high energy density and high power density, but the low thermal conductivity of organic PCMs inhibits power density by

limiting charge/discharge rates. This can be mitigated by impregnating the PCM into highly conductive CENG matrices. Here, the effect of CENG processing parameters on thermal conductivity and PCM saturation, which dictate power and energy density, were evaluated. Processing parameters included the temperature and exposure time of the heat treatment used to expand the graphite flakes.

Increasing heat treatment temperature yielded greater overall PCM saturation, as well as an increased rate of saturation. After 100 min of soaking in PCM, samples heated at 700°C were saturated 60%–70% more than samples heated at 300°C. When heat-treated at higher temperatures, SEM images showed that expanded graphite worms exhibited greater pore density, thus increasing total surface area within the matrices.

Heat treatment exposure time also influenced the rate of PCM saturation. By increasing the exposure time, the initial rate can be improved to achieve full saturation up to one day of soaking. Therefore, manufacturing processes requiring limited soaking time or heat treatment temperature could benefit from longer heating exposure time, or vice versa. If the graphite was heated longer than 30 min, or at temperatures above 500°C, the impact of exposure time diminished.

Heat treatment temperature did not affect thermal conductivity, but matrix porosity did. As porosity was increased, conductivity increased to a local maximum at around 83% porosity. This trend had been observed in past literature regardless of the parameters used to generate the CENG matrices. Further research to investigate the effect of matrix pore structure on the observed conductivity is needed.

Saturating PCM into the CENG matrix did not appear to inhibit the latent heat of fusion of the PCM. The composite latent heat of fusion was reduced proportionally to its sample mass fraction, within measured uncertainty.

Acknowledgements

This work was authored by the National Renewable Energy Laboratory, operated by Alliance for Sustainable Energy, LLC, for the U.S. Department of Energy (DOE) under contract no. DE-AC36-08GO28308. Funding provided by U.S. Department of Energy Office of Energy Efficiency and Renewable Energy Building Technologies Office. The views expressed in the article do not necessarily represent the views of the DOE or the U.S. Government.

The U.S. Government retains and the publisher, by accepting the article for publication, acknowledges that the U.S. Government retains a nonexclusive, paid-up, irrevocable, worldwide license to publish or reproduce the published form of this work, or allow others to do so, for U.S. Government purposes.

References

[1] Kim S., Drzal L.T., High latent heat storage and high thermal conductive phase change materials using exfoliated graphite nanoplatelets. Solar Energy Materials & Solar Cells, 2009, 93(1): 136–142.

[2] Lele A.F., N'Tsoukpoe K.E., Osterland T., Kuznik F., Ruck W.K., Thermal conductivity measurement of thermochemical storage materials. Applied Thermal Engineering, 2015, 89: 916–926.

[3] Chung D., A review of exfoliated graphite. Journal of Materials Science, 2016, 51(1): 554–568.

[4] Py X., Olives R., Mauran S., Paraffin/porous-graphite-matrix composite as a high and constant power thermal storage material. International Journal of Heat and Mass Transfer, 2001, 44(14): 2727–2737.

[5] Zhong Y., Li S., Wei X., Liu Z., Guo Q., Shi J., et al., Heat transfer enhancement of paraffin wax using compressed expanded natural graphite for thermal energy storage. Carbon, 2010, 48(1): 300–304.

[6] Zhao J., Guo Y., Feng F., Tong Q., Qv W., Wang H., Microstructure and thermal properties of a paraffin/expanded graphite phase-change composite for thermal storage. Renewable Energy, 2011, 36(5): 1339–1342.

[7] Ji H., Sellan D.P., Pettes M.T., Kong X., Ji J., Shi L., et al., Enhanced thermal conductivity of phase change materials with ultrathin-graphite foams for thermal energy storage. Energy & Environmental Science, 2014, 7(3): 1185–1192.

[8] Pielichowska K., Pielichowski K., Phase change materials for thermal energy storage. Progress in Materials Science, 2014, 65: 67–123.

[9] Aljehani A., Razack S.A.K., Nitsche L., Al-Hallaj S., Design and optimization of a hybrid air conditioning system with thermal energy storage using phase change composite. Energy Conversion and Management, 2018, 169: 404–418.

[10] Zalba B., Marın J.M., Cabeza L.F., Mehling H., Review on thermal energy storage with phase change: materials, heat transfer analysis and applications. Applied Thermal Engineering, 2003, 23(3): 251–283.

[11] Farid M.M., Khudhair A.M., Razack S.A.K., Al-Hallaj S., A review on phase change energy storage: materials and applications. Energy Conversion & Management, 2004, 45(9–10): 1597–1615.

[12] Nayak K., Saha S., Srinivasan K., Dutta P., A numerical model for heat sinks with phase change materials and thermal conductivity enhancers. International Journal of Heat and Mass Transfer, 2006, 49(11–12): 1833–1844.

[13] Sharma A., Tyagi V.V., Chen C., Buddhi D., Review on thermal energy storage with phase change materials and applications. Renewable and Sustainable Energy Reviews, 2009, 13(2): 318–345.

[14] Jebasingh B.E., Exfoliation of graphite by solar irradiation and investigate their thermal property on capric–myristic–palmitic acid/exfoliated graphite composite as phase change material (PCM) for energy storage. Journal of Energy Storage, 2016, 5: 70–76.

[15] Li Y., Li J., Deng Y., Guan W., Wang X., Qian T., Preparation of paraffin/porous TiO_2 foams with enhanced thermal conductivity as PCM, by covering the TiO_2 surface with a carbon layer. Applied Energy, 2016, 171: 37–45.

[16] Ibrahim N.I., Al-Sulaiman F.A., Rahman S., Yilbas B.S., Sahin A.Z., Heat transfer enhancement of phase change materials for thermal energy storage applications: A critical review. Renewable and Sustainable Energy Reviews, 2017, 74: 26–50.

[17] Goyal A., Kozubal E., Woods J., Nofal M., Al-Hallaj S., Design and performance evaluation of a dual-circuit thermal energy storage module for air conditioners. Applied Energy, 2021, 292: 116843.

[18] Woods J., Mahvi A., Goyal A., Kozubal E., Odukomaiya A., Jackson R., Rate capability and Ragone plots for phase change thermal energy storage. Nature Energy, 2021, 6(3): 295–302.

[19] Salunkhe P.B., Jaya Krishna D., Investigations on latent heat storage materials for solar water and space heating applications. Journal of Energy Storage, 2017, 12: 243–260.

[20] Guerraiche D., Bougriou C., Guerraiche K., Valenzuela L., Driss Z., Experimental and numerical study of a solar collector using phase change material as heat storage. Journal of Energy Storage, 2020, 27: 101133.

[21] Rea J.E., Toberer E.S., Siegel N.P., Guidelines for phase change material selection based on a holistic system model. Solar Energy Materials and Solar Cells, 2020, 208: 110422.

[22] Yang Z., Zhou L., Luo W., Wan J., Dai J., Han X., et al., Thermally conductive, dielectric PCM-boron nitride nanosheet composites for efficient electronic system thermal management. Nanoscale, 2016, 8(46): 19326–19333.

[23] Ali H.M., Arshad A., Janjua M.M., Baig W., Sajjad U., Thermal performance of LHSU for electronics under steady and transient operations modes. International Journal of Heat and Mass Transfer, 2018, 127: 1223–1232.

[24] Iradukunda A.-C., Kasitz J., Carlton H., Huitink D., Deshpande A., Luo F., Concurrent thermal and electrical property effects of nano-enhanced phase change material for high-voltage electronics applications. Journal of Electronic Packaging, 2020. 142(3): 031109.

[25] Zhao Y., Zou B., Li C., Ding Y., Active cooling based battery thermal management using composite phase change materials. Energy Procedia, 2019, 158: 4933–4940.

[26] Luo X., Guo Q., Li X., Tao Z., Lei S., Liu J., et al., Experimental investigation on a novel phase change material composites coupled with graphite film used for thermal management of lithium-ion batteries. Renewable Energy, 2020, 145: 2046–2055.

[27] Lei S., Shi Y., Chen G., A lithium-ion battery-thermal-management design based on phase-change-material thermal storage and spray cooling. Applied Thermal Engineering, 2020, 168: 114792.

[28] Zhao Y., Li Q., Zou B., Zhang T., Jin L., Qiao G., et al., Performance of a liquid cooling-based battery thermal management system with a composite phase change material. International Journal of Energy Research, 2020, 44(6): 4727–4742.

[29] Ling T.-C., Poon C.-S., Use of phase change materials for thermal energy storage in concrete: An overview. Construction Building Materials, 2013, 46: 55–62.

[30] Kenisarin M., Mahkamov K., Passive thermal control in residential buildings using phase change materials. Renewable and Sustainable Energy Reviews, 2016, 55: 371–398.

[31] Cai R., Sun Z., Yu H., Meng E., Wang J., Dai M., Review on optimization of phase change parameters in phase change material building envelopes. Journal of Building Engineering, 2021, 35: 101979.

[32] Lakhdari Y.A., Chikh S., Campo A., Analysis of the thermal response of a dual phase change material embedded in a multi-layered building envelope. Applied Thermal Engineering, 2020, 179: 115502.

[33] Bhamare D.K., Rathod M.K., Banerjee J., Proposal of a unique index for selection of optimum phase change material for effective thermal performance of a building envelope. Solar Energy, 2021, 218: 129–141.

[34] Sardari P.T., Grant D., Giddings D., Walker G.S., Gillott M., Composite metal foam/PCM energy store design for dwelling space air heating. Energy Conversion and Management, 2019, 201: 112151.

[35] Morovat N., Athienitis A.K., Candanedo J.A., Dermardiros V., Simulation and performance analysis of an active PCM-heat exchanger intended for building operation optimization. Energy and Buildings, 2019, 199: 47–61.

[36] Zhao C., Lu W., Tian Y., Heat transfer enhancement for thermal energy storage using metal foams embedded within phase change materials (PCMs). Solar energy, 2010, 84(8): 1402–1412.

[37] Fan L., Khodadadi J., Thermal conductivity enhancement of phase change materials for thermal energy storage: A

review. Renewable and Sustainable Energy Reviews, 2011, 15(1): 24–46.

[38] Zhao C., Wu Z., Heat transfer enhancement of high temperature thermal energy storage using metal foams and expanded graphite. Solar Energy Materials & Solar Cells, 2011, 95(2): 636–643.

[39] Zhang Q., Wang H., Ling Z., Fang X., Zhang Z., RT100/expand graphite composite phase change material with excellent structure stability, photo-thermal performance and good thermal reliability. Solar Energy Materials and Solar Cells, 2015, 140: 158–166.

[40] Sahoo S.K., Das M.K., Rath P., Application of TCE-PCM based heat sinks for cooling of electronic components: A review. Renewable and Sustainable Energy Reviews, 2016, 59: 550–582.

[41] Di Giorgio P., Iasiello M., Viglione A., Mameli M., Filippeschi S., Di Marco P., et al., Numerical analysis of a paraffin/metal foam composite for thermal storage. Journal of Physics: Conference Series, 2017, 796: 012032.

[42] Kumar N., Hirschey J., LaClair T.J., Gluesenkamp K.R., Graham S., Review of stability and thermal conductivity enhancements for salt hydrates. Journal of Energy Storage, 2019, 24: 100794.

[43] Ali H.M., Recent advancements in PV cooling and efficiency enhancement integrating phase change materials based systems—A comprehensive review. Solar Energy Materials & Solar Cells, 2020, 197: 163–198.

[44] Li C., Zhang B., Liu Q., N-eicosane/expanded graphite as composite phase change materials for electro-driven thermal energy storage. Journal of Energy Storage, 2020, 29: 101339.

[45] Mallow A., Gluesenkamp K., Abdelaziz O., Graham S., Optimization of graphite composite latent heat storage systems. ASME 2017 International Technical Conference and Exhibition on Packaging and Integration of Electronic and Photonic Microsystems collocated with the ASME 2017 Conference on Information Storage and Processing Systems. 2017. American Society of Mechanical Engineers Digital Collection, Paper No: IPACK2017-74244.

[46] Mallow A., Abdelaziz O., Graham S., Thermal charging performance of enhanced phase change material composites for thermal battery design. International Journal of Thermal Sciences, 2018, 127: 19–28.

[47] Hua J.S., Yuan C., Zhao X., Zhang J., Du J.X., Structure and thermal properties of expanded graphite/paraffin composite phase change material. Energy Sources Part A: Recovery, Utilization, and Environmental Effects, 2019, 41(1): 86–93.

[48] Mills A., Farid M., Selman J., Al-Hallaj S., Thermal conductivity enhancement of phase change materials using a graphite matrix. Applied Thermal Engineering, 2006, 26(14–15): 1652–1661.

[49] Atkin P., Farid M.M., Improving the efficiency of photovoltaic cells using PCM infused graphite and aluminium fins. Solar Energy Materials & Solar Cells, 2015, 114: 217–228.

[50] Bonnissel M., Luo L., Tondeur D., Compacted exfoliated natural graphite as heat conduction medium. Carbon, 2001, 39(14): 2151–2161.

[51] Kim J., Kim H., Kim B., Jeon K., Yoon S., Expanding characteristics of graphite in microwave-assisted exfoliation. Scientific Cooperations International Workshops on Engineering Branches, 8–9 August, 2014, Koc University, Istanbul, Turkey, pp. 273–277.

[52] Celzard A., Schneider S., Marêché J., Densification of expanded graphite. Carbon, 2002, 40(12): 2185–2191.

[53] Han J., Cho K., Lee K.-H., Kim H., Porous graphite matrix for chemical heat pumps. Carbon, 1998, 36(12): 1801–1810.

[54] Mathis N., Transient thermal conductivity measurements —comparison of destructive and non-destructive techniques. High Temperatures-High Pressures, 2000, 32(3): 321–327.

[55] Bouguerra A., Aït-Mokhtar A., Amiri O., Diop M., Measurement of thermal conductivity, thermal diffusivity and heat capacity of highly porous building materials using transient plane source technique. International Communications in Heat and Mass Transfer, 2001, 28(8): 1065–1078.

[56] Gariboldi E., Colombo L.P., Fagiani D., Li Z., Methods to characterize effective thermal conductivity, diffusivity and thermal response in different classes of composite phase change materials. Materials, 2019, 12(16): 2552.

[57] Linstrom P.J., Mallard W.G., The NIST chemistry webbook: A chemical data resource on the internet. Journal of Chemical & Engineering Data, 2001, 46(5): 1059–1063.

[58] Roberts W.L., Campbell T.J., Rapp G.R., Encyclopedia of minerals. 1990, Van Nostrand Reinhold.

[59] NIST, Standard Reference Database 69: NIST Chemistry WebBook. National Institute of Standards and Technology, 2010.

[60] Beltran V., Escardino A., Feliu C., Rodrigo M.D., Liquid suction by porous ceramic materials. British Ceramic Transactions Journal, 1988, 87(2): 64–69.

[61] Inagaki M., Nagata T., Suwa T., Toyoda M., Sorption kinetics of various oils onto exfoliated graphite. New Carbon Materials, 2006, 21(2): 97–102.

[62] Jiang H., Xu Q., Huang C., Shi L., Effect of temperature on the effective thermal conductivity of n-tetradecane-based nanofluids containing copper nanoparticles. Particuology, 2015, 22: 95–99.

[63] Balandin A.A., Thermal properties of graphene and nanostructured carbon materials. Nature Materials, 2011, 10(8): 569–581.